

# Laser Triangulation Measurements on Moving Samples With Reduced Lateral Feature Uncertainty

Thomas Kern<sup>1</sup>, Matthias Laimer<sup>1</sup>, Georg Schitter<sup>1</sup>, and Ernst Csencsics<sup>1</sup>, *Member, IEEE*

**Abstract**—This article proposes a model-based measurement correction approach for laser triangulation measurements on moving samples. A model of the laser intensity distribution on the moving sample and the obtained intensity distribution on the sensor's detector is used to decrease the motion-induced uncertainty in lateral feature width in a postprocessing step. This is achieved by detecting sharp edges, which are often feature-defining elements, with high lateral accuracy. The enhanced feature width accuracy is evaluated using an experimental laser triangulation sensor. Experimental evaluation demonstrates an improvement of 60% in lateral accuracy. Furthermore, the proposed method detects features that are missed in conventional dynamic laser triangulation measurements.

**Index Terms**—Intensity distribution model, measurement correction, measurement uncertainty, triangulation sensor.

## I. INTRODUCTION

THE industrial demand for throughput and product quality, especially in the high-tech sector, is constantly increasing [1]. With the growing need for precision, high-performance measurement systems are required [2]. Integrating measurement systems directly into the production line enables permanent quality control and a reduction of production rejects [3], [4]. Surface structure and the size of surface features frequently serve as quality criteria in such applications [5], [6]. As these surface features are often defined by edges, the edge locations have to be detected with high lateral accuracy [7].

Due to the high production speed and throughput requirements, quality inspection is performed directly on the moving sample. Hence, measurement systems combining fast measurements and high lateral resolution are required [8]. Optical measurement systems enable contactless displacement measurements with high measurement rates and are of high interest in these applications [9]. Laser triangulation sensors (LTSs) are

one of the most frequently used optical displacement sensors in industrial applications, as they combine high axial resolution with an extensive measurement range [10]. These sensors typically use CMOS imaging sensors to detect the location of the diffusely reflected laser spot [11]. The pixel values of CMOS sensors result from integrating the photocurrent caused by the incident light during the exposure time [12]. Due to this integrating behavior, a spot movement, that is, a change in the sample height, during the exposure results in a blurry image on the detector and thus increased uncertainty in the displacement measurement. Furthermore, the combination of the sensor frame rate and the sample motion causes spatial sampling of the sample's surface. Therefore, the lateral resolution of the measurement system and the detectable lateral feature size are limited [13].

Both the effect of motion blur and spatial sampling can be mitigated by decreasing the exposure time and increasing the frame rate. However, laser safety regulations in industrial manufacturing facilities are often a limiting factor for this approach [14]. Several approaches to compensate for the sample's movement have been proposed recently. Wang and Zhou [15] proposed a compensation approach for surface inspection, where the entire camera system is moving synchronized with the sample. Scanning displacement sensors, which manipulate the optical path of the sensor, were also recently introduced [16], [17]. These may also enable motion compensation with smaller actuated masses, even for higher sample velocities. While these methods can compensate for the sample movement, the actuation systems have to be reset at the end of the actuation range, rendering this approach inefficient for continuous manufacturing processes [15]. Measurement correction approaches overcome the drawbacks of mechanical actuation. However, a tailored correction approach to reduce lateral feature error in dynamic laser triangulation measurements is still missing.

The contribution of this article is a measurement correction approach to reduce feature width uncertainty in laser triangulation measurements caused by sample motion. This is achieved by analyzing the LTS' detector data and comparing it to the modeled laser intensity distribution on the moving sample's surface. In contrast to conventional laser triangulation measurements, the entire detector information is used. In Section II, the root causes of edge location uncertainty are described. The model of the intensity distribution on the

Received 7 May 2024; revised 31 July 2024; accepted 19 September 2024. Date of publication 14 October 2024; date of current version 1 November 2024. This work was supported in part by the Austrian Federal Ministry of Labor and Economy; in part by the National Foundation for Research, Technology and Development; in part by the Christian Doppler Research Association; in part by the Micro-Epsilon Atensor GmbH; and in part by the Micro-Epsilon-Messtechnik GmbH & Co.KG. The Associate Editor coordinating the review process was Dr. Lorenzo Scalise. (*Corresponding author: Thomas Kern.*)

The authors are with the Christian Doppler Laboratory for Precision Measurements in Motion, Automation and Control Institute, TU Wien, 1040 Vienna, Austria (e-mail: kern@acin.tuwien.ac.at).  
Digital Object Identifier 10.1109/TIM.2024.3480193

© 2024 The Authors. This work is licensed under a Creative Commons Attribution 4.0 License.  
For more information, see <https://creativecommons.org/licenses/by/4.0/>

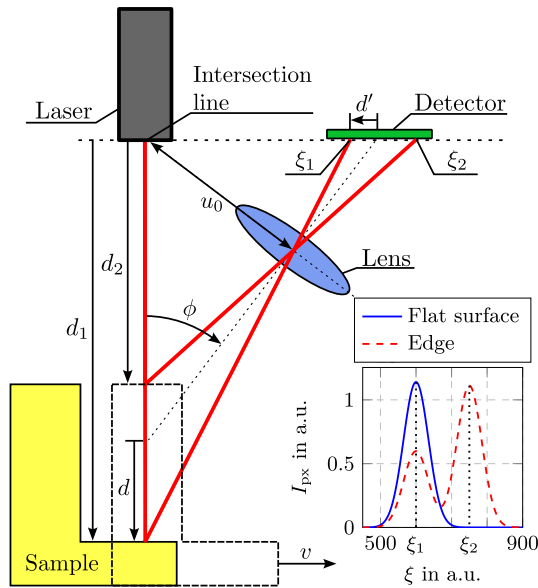


Fig. 1. Measurement principle of an LTS. The alignment of the laser source, the lens, and the detector satisfies the Scheimpflug condition. A variation of the sample height results in a displacement of the reflected laser spot on the detector. The intensity distribution on the detector is shown for a measurement on a flat surface and an edge, respectively.

imaging sensor and the sample is derived in Section III, followed by the introduction of the measurement correction algorithm in Section IV. An experimental LTS design for evaluation purposes is shown in Section V. The results of the experimental performance evaluation are presented in Section VI, and Section VII concludes the article.

## II. LATERAL FEATURE UNCERTAINTY

An exemplary LTS setup is schematically illustrated in Fig. 1 [18]. The laser source emits a beam that is diffusely reflected from the sample surface. A lens focuses the reflected spot on the detector. The geometric arrangement of the system components satisfies the Scheimpflug condition, ensuring a constant spot size on the detector over the entire measurement range [19]. An axial sample displacement  $d$  leads to a displacement  $d'$  of the reflected spot's center of gravity (COG) on the detector, following the relation [18], [20]:

$$d'(d) = \tan(\phi) f \sqrt{1 + \left( \tan(\phi) - \frac{u_0}{f} \right)^2} \times \frac{\frac{d}{\sqrt{1 + \tan(\phi)^2}}}{\left( \frac{d}{\sqrt{1 + \tan(\phi)^2}} + \frac{u_0}{\tan(\phi)} - f \right) \left( \tan(\phi) - \frac{u_0}{f} \right)} \quad (1)$$

with  $\phi$  being the triangulation angle,  $f$  the lens' focal length, and  $u_0$  the distance from the lens center to the intersection line.

LTSs typically use CMOS line sensors as detectors, as the axial sample displacement causes a 1-D spot displacement on the detector [11]. Their frame time comprises the exposure time  $T_{\text{exp}}$  and the time needed for analog-digital conversion

and readout, which is about 1% of  $T_{\text{exp}}$ . The combination of the exposure time and the sample motion yields the exposure length

$$\Delta x_{\text{exp}} = v T_{\text{exp}} \quad (2)$$

which is the distance the sample travels at velocity  $v$ . Suppose the sample surface that passes the sensor during the exposure is flat. In that case, the reflected measurement spot shows a single intensity peak on the detector as illustrated in blue in Fig. 1. If an edge passes the measurement spot during the exposure, both sample surfaces at the distances  $d_1$  and  $d_2$  contribute to the resulting intensity distribution on the detector. The spot reflections from both surfaces result in two intensity peaks at the pixel coordinates  $\xi_1$  and  $\xi_2$ . Due to the integrating behavior of the CMOS detector, the peak height corresponds to the exposure time of the respective surface. In the illustrated example in Fig. 1, the sample surface at  $d_1$  is exposed for a shorter amount of time than the surface at  $d_2$ . Thus, the peak at  $\xi_2$  is higher than at  $\xi_1$ . In such a case, conventional LTSs choose the highest peak for the displacement measurement [21], [22]. Therefore, the intensity distribution on the detector illustrated in dashed red in Fig. 1 would result in a measured value of  $d_2$ .

Omitting this part of the detector information induces lateral feature uncertainty. Fig. 2 shows an exemplary dynamic measurement of a sample feature. The reflected light from the surface during the exposure length  $\Delta x_{\text{exp}}$  yields the detector data shown in the upper plots of the figure. As illustrated, the peak height corresponds to the exposure length of the respective sample surface. Choosing the highest peak as in conventional measurements results in the red data points. As the displacement measurement of a data point corresponds to the exposed sample length before the lateral position of the data point (see Fig. 2), the measured feature appears shifted toward positive  $x_s$  values. The smallest lateral feature error is achieved by measuring the feature width exactly between two measurement points as illustrated. However, due to the spatial sampling, the measured feature width  $w_m$  discretely changes in intervals of  $\Delta x_{\text{exp}}$ , defining the lateral resolution of the LTS in conventional dynamic measurements. Since sample features are of arbitrary size, the lateral resolution induces uncertainty in the measured feature width. Furthermore, if the feature width  $w$  and the exposure length  $\Delta x_{\text{exp}}$  fulfill the condition  $w < \Delta x_{\text{exp}}$ , features can be missed in conventional dynamic measurements, which limits the lateral spatial resolution.

## III. LASER INTENSITY DISTRIBUTION MODEL

The incident laser intensity distribution on the sample is deterministic, and assuming a constant reflectivity of the sample, the peak power on the detector corresponds to the exposure time of the respective surface. Therefore, the lateral feature accuracy can be refined by modeling the intensity distribution. To determine the ratio of the reflected power from the sample surfaces, the intensity distribution obtained by the detector is analyzed using 1-D Gaussian maximum likelihood estimation (MLE) [23], [24], matched filtering [25], [26], and Gaussian mixture models (GMMs) [27].

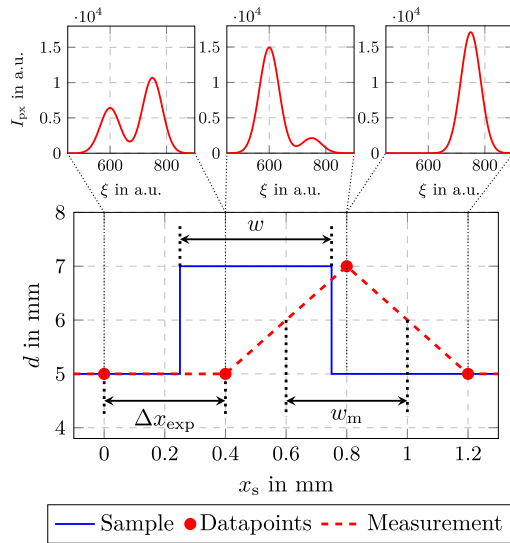


Fig. 2. Exemplary measurement result of a conventional measurement in motion. Choosing the highest intensity peak results in the red data points.

### A. One-Dimensional Gaussian Model

As the laser source emits a Gaussian beam, the resulting intensity distribution on the detector when measuring on a flat surface is of Gaussian shape as well. Thus, the obtained data from the imaging sensor can be described as the 1-D Gaussian distribution

$$\mathcal{N}(\xi|\mu, \sigma) = \frac{1}{\sigma\sqrt{2\pi}} e^{-\frac{1}{2}\left(\frac{\xi-\mu}{\sigma}\right)^2} \quad (3)$$

with  $\xi$  being the pixel coordinate,  $\mu$  the mean value, and  $\sigma$  the standard deviation. The parameters  $\mu$  and  $\sigma$  are determined using MLE [23], [24] as

$$\mu = \frac{1}{P_{tot}} \sum_{n=1}^N I_{px}(\xi_n) \xi_n \quad (4a)$$

$$\sigma = \frac{1}{P_{tot}} \sum_{n=1}^N I_{px}(\xi_n) (\xi_n - \mu)^2 \quad (4b)$$

for  $N$  pixels with the pixel values  $I_{px}$  of the respective pixel coordinates  $\xi_n$ , and the total power

$$P_{tot} = \sum_{n=1}^N I_{px}(\xi_n). \quad (5)$$

The mean  $\mu$  of the Gaussian model is equivalent to the spot's COG and used to determine the distance to the sample  $d$  as discussed in Section V.

While the 1-D Gaussian model fits the obtained data well for measurements on flat surfaces, it is unsuitable for measurements on edges, as the intensity distribution is no longer Gaussian. An example of the resulting intensity distribution when an edge passes the laser during exposure is given in Fig. 3. Two intensity peaks are visible, with their peak locations corresponding to the sample heights on either side of the edge.

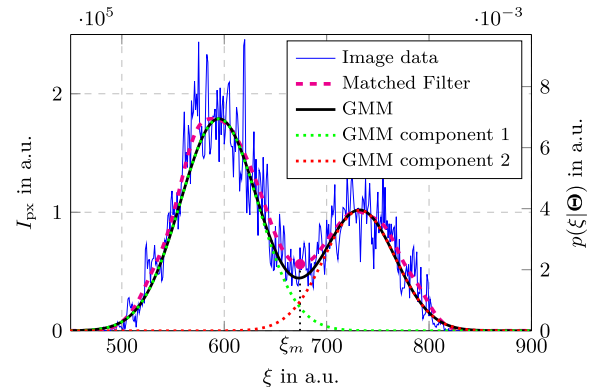


Fig. 3. Intensity distribution of a static measurement conducted on an edge. The distribution is described by fitting a GMM to the data and by matched filtering.

### B. Matched Filtering

The relative peak power can be determined by summation of the pixel intensity values  $I_{px}(\xi_n)$  of the respective peak and normalization by the total power  $P_{tot}$

$$P_1 = \frac{\sum_{n=1}^m I_{px}(\xi_n)}{P_{tot}} \quad (6a)$$

$$P_2 = \frac{\sum_{n=m+1}^N I_{px}(\xi_n)}{P_{tot}} \quad (6b)$$

with  $m$  being the index of the pixel coordinate at the local minimum between the peaks. However, determining the local minimum  $\xi_m$  is sensitive to noise. Since the shape of an intensity peak on the detector is expected to be Gaussian, a matched filter with a Gaussian filter kernel  $\mathcal{N}(\mathbf{X}_f|\mu_f, \sigma_f)$  is used to denoise the obtained intensity distribution [25], [26]. To avoid overlaps between the filter kernel and a second peak, the filter's standard deviation  $\sigma_f$  is chosen three times smaller than a single peak's standard deviation  $\sigma$ . Furthermore, the filter is zero centered  $\mu_f = 0$  and has a width of  $\mathbf{X}_f = [-4\sigma_f, \dots, 4\sigma_f]^T$ . The vector of filtered intensity values  $\mathbf{I}_f(\xi)$  is derived by

$$\mathbf{I}_f(\xi) = \mathcal{F}^{-1}\{\mathcal{F}\{\mathbf{I}_{px}(\xi)\} \mathcal{F}^*\{\mathcal{N}(\mathbf{X}_f|\mu_f, \sigma_f)\}\} \quad (7)$$

with  $\mathcal{F}$  denoting the Fourier transform of the respective vectors. The denoised intensity distribution illustrated in Fig. 3 fits the raw intensity distribution well, and the local minimum between the two peaks can be identified. If, due to excessive noise, multiple local minima are found, the minimum showing the highest prominence is chosen [28]. To achieve subpixel accuracy, the Gaussian interpolation [29], [30]

$$\zeta = \frac{\ln(\xi_{max} - 1) - \ln(\xi_{max} + 1)}{2[\ln(\xi_{max} + 1) - 2\ln(\xi_{max}) + \ln(\xi_{max} - 1)]} \quad (8)$$

with the pixel coordinate of the maximum intensity

$$\xi_{max} = \underset{\xi}{\operatorname{argmax}} I_f(\xi) \quad (9)$$

is applied to obtain the highest peak's pixel coordinate  $\zeta$ .

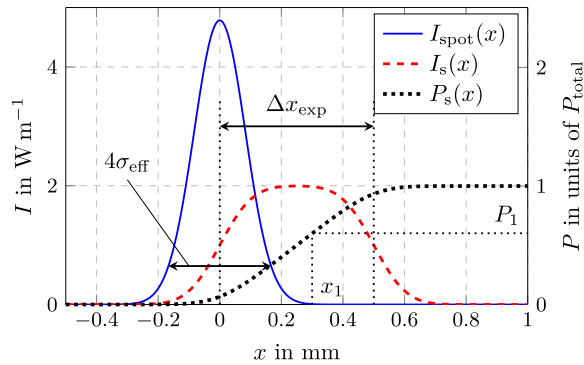


Fig. 4. Modeled intensity and power distribution on the sample surface. The intensity of the sample is described by a convolution of the Gaussian spot profile over the distance traveled during the exposure time. Integrating the intensity distribution yields the normalized power.

### C. Gaussian Mixture Model

For a small second peak, a local minimum with sufficient prominence cannot always be found in the filtered intensity distribution. Hence, a GMM [27] is used in that case. It describes the intensity distribution as a weighted superposition of Gaussian distributions

$$p(\xi|\Theta) = \sum_{k=1}^K \pi_k \mathcal{N}(\xi|\mu_k, \sigma_k) \quad (10)$$

with  $K$  being the Gaussian components, their respective weights  $\pi_k$  and the parameter vector

$$\Theta = [\Theta_1^T, \dots, \Theta_K^T]^T = [\mu_1, \sigma_1, \pi_1, \dots, \mu_K, \sigma_K, \pi_K]^T. \quad (11)$$

The weights fulfill the relation

$$\sum_{k=1}^K \pi_k = 1 \quad (12)$$

such that the overall distribution given in (10) has a total power of 1. The estimation of the model parameters  $\Theta$  is performed by the iterative expectation-maximization (EM) algorithm for GMM [31], [32], [33]. As the framerate of the imaging sensor is considered to be sufficiently high, that is, that only one edge is passing by the sensor during one exposure time, a GMM consisting of two Gaussian components,  $K = 2$ , is chosen.

The E-step and M-step are iterated until the loglikelihood improves less than a chosen threshold. Using the obtained model, the pixel coordinates of the peaks are obtained by solving

$$\zeta_{1,2} = \underset{\xi}{\operatorname{argmin}} \{-p(\xi|\Theta)\}, \quad \xi_0 = \mu_{1,2}. \quad (13)$$

As the GMM is normalized to a total power of 1 and each component, excluding the weighting factors, has a total power of 1 as well, the component weights  $\pi_1, \pi_2$  directly correspond to the relative peak powers, respectively.

### D. Laser Intensity Distribution on the Sample

While the intensity distribution on the detector is used to determine the ratio of the reflected laser power, it does not contain spatial feature width information. To link the determined reflected power ratio to the lateral feature width, the laser intensity and power distribution on the sample are modeled.

The collimated laser beam has a Gaussian intensity profile

$$I_{\text{spot}}(x, y) = \frac{1}{2\pi\sigma^2} e^{-\frac{1}{2} \frac{(x-x_0)^2 + (y-y_0)^2}{\sigma^2}} \quad (14)$$

with  $x, y$  being the lateral coordinates,  $x_0, y_0$  the spot center, and  $\sigma$  the spot's standard deviation. As the spot has circular symmetry and edges are assumed to occur perpendicular to the direction of motion, a 1-D intensity distribution

$$I_{\text{spot}}(x) = \int_{-\infty}^{\infty} I_{\text{spot}}(x, y) dy = \frac{1}{\sigma\sqrt{2\pi}} e^{-\frac{(x-x_0)^2}{2\sigma^2}} \quad (15)$$

is used. The waist diameter of the beam is defined as the  $1/e^2$  diameter, which corresponds to a beamwidth of  $4\sigma$ . As the outer regions of the spot are due to their low intensity not detectable by the detector, the effective spot width  $4\sigma_{\text{eff}}$ , depending on the laser power, the sample's reflectivity, and the detector's exposure time, is used in the model.

The CMOS imaging sensor's pixel values correspond to the integrated intensity of the incident light during one exposure time. Therefore, the intensity distribution on the sensor equals the mean intensity reflected from the sample surface over one exposure length  $\Delta x_{\text{exp}}$

$$I_s(x) = \frac{1}{\Delta x_{\text{exp}}} \int_{x_0}^{x_0 + \Delta x_{\text{exp}}} \frac{1}{\sigma_{\text{eff}}\sqrt{2\pi}} e^{-\frac{(x-x_0-\tau)^2}{2\sigma_{\text{eff}}^2}} d\tau = \frac{\operatorname{erf}\left(\frac{\sqrt{2}(x-2x_0)}{2\sigma_{\text{eff}}}\right) + \operatorname{erf}\left(\frac{\sqrt{2}(2x_0 + \Delta x_{\text{exp}} - x)}{2\sigma_{\text{eff}}}\right)}{2\Delta x_{\text{exp}}} \quad (16)$$

with  $x_0$  being the lateral coordinate at the start of the exposure and  $\operatorname{erf}()$  the error function. The intensity distribution  $I_s(x)$  is normalized to have a total power of 1. Fig. 4 illustrates the resulting intensity distribution. To determine the normalized power on the sample until a point  $x$ , the intensity distribution is integrated along the direction of motion as

$$P_s(x) = \int_{-\infty}^x I_s(\tau) d\tau = \frac{\sigma_{\text{eff}}(e^{-\alpha^2} - e^{-\beta^2})}{\sqrt{2\pi}\Delta x_{\text{exp}}} + \frac{(x-2x_0)\operatorname{erf}(\alpha) + (x-2x_0-\Delta x_{\text{exp}})\operatorname{erf}(\beta) + \Delta x_{\text{exp}}}{2\Delta x_{\text{exp}}} \quad (17)$$

with the coefficients

$$\alpha = \frac{x-2x_0}{\sqrt{2}\sigma_{\text{eff}}} \quad (18a)$$

$$\beta = \frac{-x+2x_0+\Delta x_{\text{exp}}}{\sqrt{2}\sigma_{\text{eff}}}. \quad (18b)$$

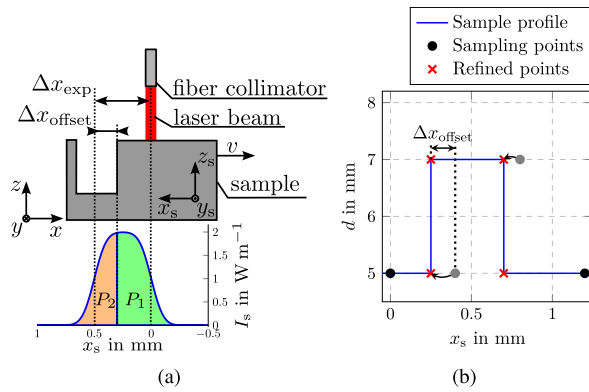


Fig. 5. Schematic illustration of the laser power distribution and sampling point refinement when measuring on a moving sample. (a) Intensity distribution on the sample and the relative powers  $P_1$  and  $P_2$ . (b) Measurement result. The gray sampling points result from a conventional measurement, while the red crosses mark the refined sampling points.

#### IV. MODEL-BASED FEATURE WIDTH REFINEMENT

Using the models shown above, a feature width refinement method, tailored to detect edge locations, is introduced. A schematic illustration of a dynamic measurement on a sample feature is given in Fig. 5(a). As the sample is moving with a velocity  $v$  in the  $x$ -direction, the laser is moving in the  $x_s$ -direction in the sample fixed coordinate system  $[x_s, y_s, z_s]^T$ . The sample motion leads to the illustrated intensity distribution on the sample according to (16), with the relative power  $P_1$  before the edge and  $P_2$  after the edge, as shown in (17). In a conventional measurement, the highest peak is used to determine the sample displacement as discussed in Section II. As  $P_1$  is larger than  $P_2$  in the illustrated case, the intensity peak corresponding to  $P_1$  would be used, leading to a displacement value equal to the displacement before the edge as depicted in Fig. 5(b). This causes a lateral shift of the assumed edge location and, therefore, feature width uncertainty. By determining the relative reflected power  $P_2$ , the corresponding lateral offset  $\Delta x_{\text{offset}}$  can be determined using the power distribution derived in (17).

The detector data must be preprocessed in the first step to determine the relative powers and sample displacement. Algorithm 1 applies the models introduced in Section III to minimize computational effort. First, the matched filter is applied to the raw intensity distribution, as it is the computationally cheapest method. If no prominent local minimum is found, a 1-D Gaussian function is fit to the intensity distribution. As the GMM is the computationally most expensive algorithm, it is only applied if the spot width of the 1-D model exceeds the threshold of  $\sigma = 50$ , indicating that a double peak could be present. The displacement  $d$  is obtained using a calibration model  $\mathcal{M}(\zeta)$  introduced in Section V.

As the relative powers are estimated, the lateral edge offset  $\Delta x_{\text{offset}}$  is determined by solving

$$P_s(\Delta x_{\text{offset}})|_{x_0=0} - P_2 = 0 \quad (19)$$

for  $\Delta x_{\text{offset}}$ . To refine the feature width, the lateral coordinate  $x_s$  of the sampling point is shifted by  $-\Delta x_{\text{offset}}$ . The

#### Algorithm 1 Measurement Data Preprocessing

---

**Require:**  $I_{\text{px}}(\xi)$   
**Ensure:**  $d, P_1, P_2$

```

 $I_f(\xi) \leftarrow$  matched filter Eq. (7)
 $[\xi_{m_1}, \dots, \xi_{m_M}]^T \leftarrow$  local minima of  $I_f(\xi)$ 
if  $M > 0$  then {Local minima found}
    if  $M > 1$  then {Multiple local minima found}
         $\xi_m \leftarrow$  argmax prominence( $I(\xi_{m_1, \dots, m_M})$ )
    end if
     $P_1, P_2 \leftarrow$  Eq. (6)
     $\zeta \leftarrow$  Eq. (8)
else {No local minimum found, fit 1D Gaussian}
     $\mu, \sigma \leftarrow$  Eq. (4)
    if  $\sigma \leq 50$  then {Spotwidth exceeds threshold}
         $\Theta \leftarrow$  GMM EM-algorithm
         $P_1 \leftarrow \pi_1$ 
         $P_2 \leftarrow \pi_2$ 
         $\zeta_{1,2} \leftarrow$  Eq. (13)
         $\zeta \leftarrow$  argmax $_{\zeta_{1,2}} p(\zeta_{1,2} | \Theta)$ 
    else {No edge detected}
         $P_1, P_2 \leftarrow 0$ 
         $\zeta \leftarrow \mu$ 
    end if
end if
 $d \leftarrow \mathcal{M}(\zeta)$  {Obtain displacement from peak location}
return  $d, P_1, P_2$ 

```

---

displacement value obtained by the next sampling point is copied and inserted at the same lateral position as the previously refined point to indicate a sharp edge, as illustrated in Fig. 5(b).

#### V. EXPERIMENTAL SENSOR DESIGN

For evaluating the proposed method, an experimental LTS is designed. The geometric alignment is illustrated in Fig. 6(a). The setup is aligned to fulfill the Scheimpflug and Hinge conditions, ensuring a constant spot size over the entire measurement range [34]. Fig. 6(b) shows the assembled LTS with all its components. A solid-state laser (PL206, Thorlabs, USA) with a wavelength of 638.8 nm is coupled into an optical fiber (P1-630A-FC-2, Thorlabs, USA). Using a fiber collimator (F230FC-B, Thorlabs, USA), a collimated beam with a waist diameter of  $w = 0.8$  mm is emitted and aligned perpendicular to the sample surface. A bi-convex lens (LB1761-A-ML, Thorlabs, USA) with a focal length of  $f = 25.4$  mm focuses the diffusely reflected spot on the 2-D imaging sensor (DMM 37UX273-ML, The Imaging Source, USA) which is connected to the computer via USB3.0 interface. The choice of a 2-D imaging sensor is deliberately made to compensate for rotational misalignments of the imaging sensor and the fiber collimator.

As the reflected spot on the detector moves along a straight line, the 2-D data is transformed into 1-D data. A position-controlled vertical stage (X-VSR20A-SV2, Zaber, Canada) is used to identify the principal axis of the spot's motion on the sensor. Using principal component analysis (PCA), a transformation vector  $\mathbf{w}$  is derived [35], [36]. The transformed 1-D

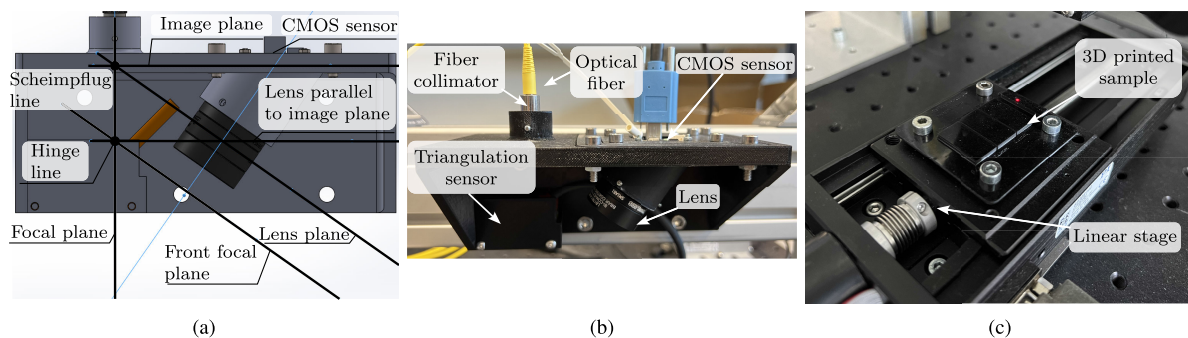


Fig. 6. Experimental setup. (a) CAD model of the experimental LTS, which satisfies both the Scheimpflug and the Hinge condition. (b) Experimental setup. (c) Sample which is actuated by a linear stage.

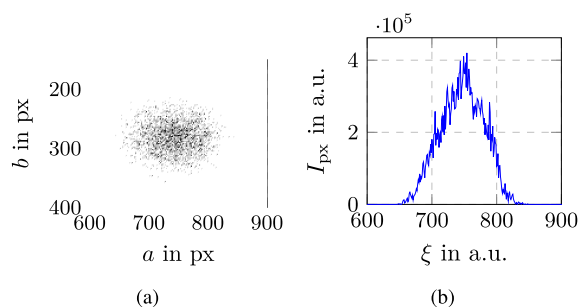


Fig. 7. Dimensionality reduction of the detector data. (a) Raw data obtained by the 2-D imaging sensor. (b) Transformed 1-D data.

pixel coordinates  $\xi$  result in

$$\xi = \mathbf{w}^T \mathbf{X}, \quad \xi \in \mathbb{R}^{1 \times N}, \mathbf{w} \in \mathbb{R}^2, \mathbf{X} \in \mathbb{R}^{2 \times N} \quad (20)$$

with  $\mathbf{w}$  being the transformation vector,  $\mathbf{X}$  the vector of 2-D pixel coordinates, and  $N$  the total number of pixels. The resulting pixel coordinates are binned to equidistant whole-numbered pixel values. Fig. 7(b) shows the resulting sensor data obtained from the 2-D image given in Fig. 7(a). As can be seen, the 1-D intensity distribution can be approximated by a Gaussian curve.

The experimental LTS is calibrated using an industrial LTS (optoNCDT1420, Micro-Epsilon, Germany) and the vertical stage. By mapping the COG  $\zeta$  of the obtained intensity distribution on the detector to the stage displacement  $d$  measured by the industrial LTS, a cubic spline model [37]

$$d = \mathcal{M}(\zeta) \quad (21)$$

is fit to the obtained data.

## VI. EXPERIMENTAL RESULTS

The experimental evaluation is performed on a 3-D-printed test sample. A precision linear stage (VT-80, Physik Instrumente GmbH and Co.KG, Germany) with a top speed of  $v = 20 \text{ mm s}^{-1}$  and a step size of  $1 \mu\text{m}$  is used to actuate the test sample as displayed in Fig. 6(c). The sample shows trench features with a depth of 2 mm and varying widths. As a reference measurement, the sample topography is determined

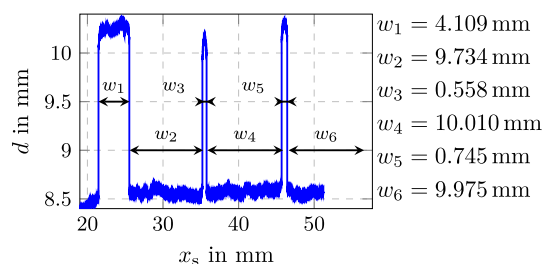


Fig. 8. Reference measurement of the 3-D printed sample. The sample consists of six features with varying widths.

by conducting static measurements with a lateral sampling of  $1 \mu\text{m}$ . The reference measurement showing three trenches with the corresponding feature widths is illustrated in Fig. 8.

The result of a corrected measurement at a sample speed of  $v = 20 \text{ mm s}^{-1}$  and an exposure time of  $T_{\text{exp}} = 40 \text{ ms}$  resulting in an exposure length of  $\Delta x_{\text{exp}} = 0.8 \text{ mm}$  is shown in Fig. 9. As can be seen in the conventional measurement, the features appear shifted to positive  $x_s$  values, which corresponds to the expected effects discussed in Section II and Fig. 2. The feature at  $x_s = 35.5 \text{ mm}$  is missed in the conventional measurement. Since the feature width is smaller than the exposure length, the highest peaks in the detector data correspond to the sample surfaces before and after the feature. The feature at  $x_s = 46.5 \text{ mm}$  is detected. However, the lateral feature resolution is limited to the exposure length in the conventional measurement. Applying the proposed method, the edge locations and, thus, the feature widths are estimated using the full information contained in the detector's intensity distribution. As shown in Fig. 9, the correction approach refines the features with high accuracy.

To quantify the correction performance, measurements at a sample speed of  $v = 20 \text{ mm s}^{-1}$  and exposure times ranging from 10 to 50 ms leading to exposure lengths in the range of  $\Delta x_{\text{exp}} = 0.2, \dots, 1 \text{ mm}$  are performed. For each configuration of  $\Delta x_{\text{exp}}$ , 50 measurements with random sample starting positions are conducted, where the measured feature widths  $w_1$  to  $w_6$  serve as evaluation criteria. The lateral edge locations and, thus, the feature widths are well-defined in the refined measurements, as two data points are placed at the same lateral

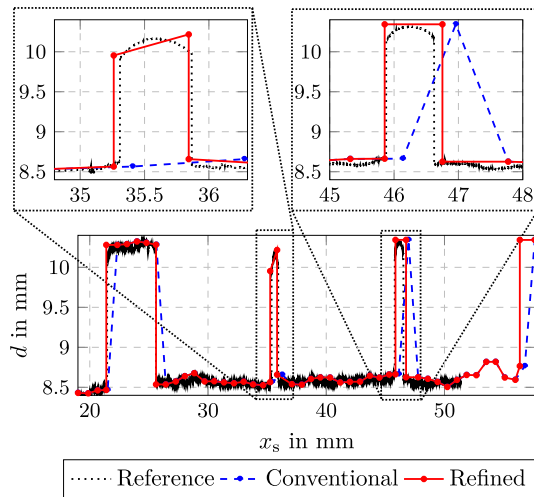


Fig. 9. Experimental result of a corrected measurement at a travel distance of  $\Delta x_{\text{exp}} = 0.8$  mm. The missed feature at  $x_s = 35.5$  mm is reconstructed, and the lateral edge location accuracy is refined.

TABLE I

COMPARISON OF FEATURE WIDTH ERRORS FOR CONVENTIONAL AND REFINED MEASUREMENTS. FOR EACH  $\Delta x_{\text{exp}}$  CONFIGURATION, 50 MEASUREMENTS WITH RANDOM STARTING POSITIONS ARE CONDUCTED. CONVENTIONAL RESULTS ARE DENOTED WITH SUBSCRIPT “c” AND REFINED VALUES WITH SUBSCRIPT “r”

$\Delta x_{\text{exp}}$ in mm	0.2	0.4	0.6	0.8	1.0
$ e_c $ in $\mu\text{m}$	74.3	145.0	180.6	238.8	353.7
$ e_r $ in $\mu\text{m}$	23.6	58.7	68.5	151.1	244.7
$\sigma_{e_c}$	90.5	175.2	224.2	351.6	464.1
$\sigma_{e_r}$	29.4	85.9	84.1	184.3	286.5
missed <sub>c</sub>	0	0	4	19	31
missed <sub>r</sub>	0	0	0	0	13

position to indicate an edge. In conventional measurements, the edge locations are assumed to be at the lateral position exactly between the two edge-defining sample points to enable a fair comparison.

Considering the mean absolute errors and the standard deviations given in Table I, it is visible that the feature width uncertainty increases with increasing exposure length  $\Delta x_{\text{exp}}$ . Applying the proposed method significantly reduces the mean absolute feature width error  $|e|$  and its standard deviation  $\sigma_e$ . The correction approach reduces the mean absolute feature width error by more than 60% for the configurations where no features are missed in the conventional measurement. For the case where features get missed in the conventional measurement, the correction still reduces the uncertainty by almost 40%.

As mentioned above, features can be missed in the conventional measurement if the feature width is smaller than the exposure length. Thus, as shown in Table I, for a travel distance of  $\Delta x_{\text{exp}} = 0.6$  mm feature  $w_3$  gets missed in four of the 50 measurements. The correction approach shows a significant improvement, as the first missed features appear at  $\Delta x_{\text{exp}} = 1$  mm. As long as at least one sampling point is

located on the feature, that is, the feature’s edges appear in the detector data during two exposures, the proposed method can detect the feature width with high lateral accuracy.

In summary, the experimental evaluation shows that the proposed method successfully reduces lateral feature width uncertainty and detects features that are missed in conventional dynamic measurements.

## VII. CONCLUSION AND OUTLOOK

This article presents an offline measurement correction approach to enhance the feature width accuracy for laser triangulation measurements on moving samples. For this purpose, a measurement correction algorithm is developed to estimate the lateral edge location between two measurement points and, therefore, the feature widths. The relative reflected peak powers are calculated using a combination of matched filtering, 1-D Gaussian MLE, and GMM. The feature width defining lateral edge locations is estimated by comparing this power ratio to the modeled intensity distribution on the sample. Due to the lateral relocation of sampling points, the proposed method results in nonequidistant sampling points. Experimental evaluation shows a significant feature width uncertainty reduction of more than 60%. Furthermore, missed features with a width in the size of the exposure length are detected, and feature width is determined with high accuracy using the proposed method.

Considering implementation in real industrial applications, system parameters such as exposure time and laser spot size have to be chosen appropriately for the expected feature widths and sample velocity. The effective spot size  $4\sigma_{\text{eff}}$  has to be smaller than the smallest expected feature width, to unambiguously detect the feature’s edges. As the exposure length  $\Delta x_{\text{exp}}$  is the performance defining parameter, the exposure time  $T_{\text{exp}}$  has to be scaled according to (2) for the given sample velocity  $v$ .

## REFERENCES

- [1] S. Sahoo and C.-Y. Lo, “Smart manufacturing powered by recent technological advancements: A review,” *J. Manuf. Syst.*, vol. 64, pp. 236–250, Jul. 2022.
- [2] X. Jiang and D. J. Whitehouse, “Precision metrology,” *Philos. Trans. Roy. Soc. A, Math., Phys. Eng. Sci.*, vol. 370, no. 1973, pp. 4154–4160, Aug. 2012.
- [3] V. Azamfirei, F. Psarommatis, and Y. Lagrosen, “Application of automation for in-line quality inspection, a zero-defect manufacturing approach,” *J. Manuf. Syst.*, vol. 67, pp. 1–22, Apr. 2023.
- [4] G. Fragapane, R. Eleftheriadis, D. Powell, and J. Antony, “A global survey on the current state of practice in zero defect manufacturing and its impact on production performance,” *Comput. Ind.*, vol. 148, Jun. 2023, Art. no. 103879.
- [5] T.-F. Yao, A. Duennen, and M. Cullinan, “In-line dimensional metrology in nanomanufacturing systems enabled by a passive semiconductor wafer alignment mechanism,” *J. Micro Nano-Manuf.*, vol. 5, no. 1, Mar. 2017, Art. no. 011001.
- [6] A. Yogeswaran and P. Payeur, “3D surface analysis for automated detection of deformations on automotive body panels,” in *New Advances in Vehicular Technology and Automotive Engineering*. Rijeka, Croatia: InTech, 2012, pp. 953–978.
- [7] D. J. Whitehouse, *Handbook of Surface and Nanometrology*. FL, USA: Taylor & Francis, 2002.
- [8] K. Maize, Y. Mi, M. Cakmak, and A. Shakouri, “Real-time metrology for roll-to-roll and advanced inline manufacturing: A review,” *Adv. Mater. Technol.*, vol. 8, no. 2, Jan. 2023, Art. no. 2200173.

- [9] G. Sansoni, M. Trebeschi, and F. Docchio, "State-of-the-art and applications of 3D imaging sensors in industry, cultural heritage, medicine, and criminal investigation," *Sensors*, vol. 9, no. 1, pp. 568–601, Jan. 2009.
- [10] L. Traxler, L. Ginner, S. Breuss, and B. Blaschitz, "Experimental comparison of optical inline 3D measurement and inspection systems," *IEEE Access*, vol. 9, pp. 53952–53963, 2021.
- [11] M. A. Drouin and J. A. Beraldin, "Active triangulation 3D imaging systems for industrial inspection," in *3D Imaging, Analysis and Applications*, 2nd ed. Switzerland: Springer, Jan. 2020, pp. 109–165.
- [12] A. El Gamal and H. Eltoukhy, "CMOS image sensors," *IEEE Circuits Devices Mag.*, vol. 21, no. 3, pp. 6–20, May 2005.
- [13] A. Cigada, F. Mancosu, S. Manzoni, and E. Zappa, "Laser-triangulation device for in-line measurement of road texture at medium and high speed," *Mech. Syst. Signal Process.*, vol. 24, no. 7, pp. 2225–2234, Oct. 2010.
- [14] *Safety of Laser Products—Part 1: Equipment Classification and Requirements*, Standard EN 60825-1:2014/AC:2022-03, Brussels, Belgium, 2014.
- [15] X. Wang and Y. Zhou, "A mechanical transmission based image de-blurring method used for on-line surface quality inspection," *Measurement*, vol. 151, Feb. 2020, Art. no. 107262.
- [16] J. Schlarp, E. Csencsics, and G. Schitter, "Design and evaluation of an integrated scanning laser triangulation sensor," *Mechatronics*, vol. 72, Dec. 2020, Art. no. 102453.
- [17] D. Wertjan, T. Kern, E. Csencsics, G. Stadler, and G. Schitter, "Compact scanning confocal chromatic sensor enabling precision 3-D measurements," *Appl. Opt.*, vol. 60, no. 25, pp. 7511–7517, 2021.
- [18] A. Donges and R. Noll, *Laser Measurement Technology: Fundamentals and Applications*, 1st ed., Berlin, Germany: Springer, 2015.
- [19] T. Scheimpflug, "Improved method and apparatus for the systematic alteration or distortion of plane pictures and images by means of lenses and mirrors for photography and for other purposes," British Patent 1196 (Great Britain), 1904.
- [20] E. Csencsics, J. Schlarp, T. Glaser, T. Wolf, and G. Schitter, "Reducing the speckle-induced measurement uncertainty in laser triangulation sensors," *IEEE Trans. Instrum. Meas.*, vol. 72, pp. 1–9, 2023.
- [21] *ILD1900-2-IE Operating Instructions optoNCDT 1900 EtherCAT*, Micro-Epsilon, Ortenburg, Germany, 2024.
- [22] *Operating Instructions optoNCDT 1420*, Micro-Epsilon, Ortenburg, Germany, 2024.
- [23] C. M. Bishop, *Pattern Recognition and Machine Learning*, 1st ed., New York, NY, USA: Springer, Aug. 2006.
- [24] I. J. Myung, "Tutorial on maximum likelihood estimation," *J. Math. Psychol.*, vol. 47, no. 1, pp. 90–100, Feb. 2003.
- [25] G. Turin, "An introduction to matched filters," *IEEE Trans. Inf. Theory*, vol. IT-6, no. 3, pp. 311–329, Jun. 1960.
- [26] G. L. Turin, "An introduction to digital matched filters," *Proc. IEEE*, vol. 64, no. 7, pp. 1092–1112, Jul. 1976.
- [27] D. A. Reynolds, "Gaussian mixture models," *Encyclopedia Biometrics*, vol. 741, nos. 659–663, pp. 659–663, 2009.
- [28] C. Will, K. Shi, R. Weigel, and A. Koelpin, "Advanced template matching algorithm for instantaneous heartbeat detection using continuous wave radar systems," in *IEEE MTT-S Int. Microw. Symp. Dig.*, May 2017, pp. 1–4.
- [29] H. Nobach and M. Honkanen, "Two-dimensional Gaussian regression for sub-pixel displacement estimation in particle image velocimetry or particle position estimation in particle tracking velocimetry," *Experim. Fluids*, vol. 38, no. 4, pp. 511–515, Apr. 2005.
- [30] C. E. Willert and M. Gharib, "Digital particle image velocimetry," *Exp. Fluids*, vol. 10, no. 4, pp. 181–193, 1991.
- [31] J. A. Bilmes, "A gentle tutorial of the EM algorithm and its application to parameter estimation for Gaussian mixture and hidden Markov models," *Int. Comput. Sci. Inst.*, vol. 4, p. 126, Jan. 1998.
- [32] A. P. Dempster, N. M. Laird, and D. B. Rubin, "Maximum likelihood from incomplete data via the EM algorithm," *J. Royal Stat. Soc. B, Methodol.*, vol. 39, no. 1, pp. 1–22, 1977.
- [33] G. Xuan, W. Zhang, and P. Chai, "EM algorithms of Gaussian mixture model and hidden Markov model," in *Proc. Int. Conf. Image Process.*, vol. 1, 2001, pp. 145–148.
- [34] H. M. Merklinger, *Focusing the View Camera*, vol. 5. Dartmouth, NS, Canada: Seaboard Printing, 1996.
- [35] M. Partridge and R. A. Calvo, "Fast dimensionality reduction and simple PCA," *Intell. Data Anal.*, vol. 2, no. 3, pp. 203–214, Jul. 1998.
- [36] B. M. S. Hasan and A. M. Abdulazeez, "A review of principal component analysis algorithm for dimensionality reduction," *J. Soft Comput. Data Mining*, vol. 2, no. 1, pp. 20–30, 2021.
- [37] S. Durrleman and R. Simon, "Flexible regression models with cubic splines," *Statist. Med.*, vol. 8, no. 5, pp. 551–561, May 1989.



**Thomas Kern** received the M.Sc. degree in electrical engineering from TU Wien, Vienna, Austria, in 2024.

He is a Doctoral Researcher at the Automation and Control Institute (ACIN), TU Wien. His primary research interests include optical inline measurement systems and precision measurements in motion.



**Matthias Laimer** received the M.Sc. degree in electrical engineering from TU Wien, Vienna, Austria, in 2022.

He is a Doctoral Researcher at the Automation and Control Institute (ACIN), TU Wien. His primary research interests include optical high-speed sensing for industrial automation.



**Georg Schitter** received the M.Sc. degree in electrical engineering from TU Graz, Graz, Austria, in 2000, and the M.Sc. and Ph.D. degrees from ETH Zurich, Zurich, Switzerland, in 2004.

He is a Professor of advanced mechatronic systems at the Automation and Control Institute (ACIN), TU Wien, Vienna, Austria. His primary research interests include high-performance mechatronic systems, particularly for applications in the high-tech industry, scientific instrumentation, and mechatronic imaging systems, such as AFM, scanning laser and LiDAR systems, telescope systems, adaptive optics, and lithography systems for the semiconductor industry.



**Ernst Csencsics** (Member, IEEE) received the M.Sc. and Ph.D. degrees (Hons.) in electrical engineering from TU Wien, Vienna, Austria, in 2014 and 2017, respectively.

He is an Associate Professor of measurement systems at the Automation and Control Institute (ACIN), TU Wien. His primary research interests include opto-mechatronic measurement and imaging systems, high-performance mechatronics, scientific instrumentation, precision engineering, and advanced robotic inline measurement systems.

Dr. Csencsics received the Journal Best Paper Award of IEEE/ASME TRANSACTIONS ON MECHATRONICS in 2018, the Best Paper Award at the IEEE International Instrumentation and Measurement Technology Conference in 2022, and the Best Student Paper Award at the American Control Conference in 2016.